Atomic Structure and Electrical Activity of Grain Boundaries and Ruddlesden-Popper Faults in Cesium Lead Bromide Perovskite

Arashdeep Singh Thind,[†,#] Guangfu Luo,[‡,#] Jordan A. Hachtel,[§] Maria V. Morrell,[∥] Sung Beom Cho,[‡] Albina Y. Borisevich,[⊥] Juan-Carlos Idrobo,[§] Yangchuan Xing,[∥] and Rohan Mishra[,‡,†]*

[†]Institute of Materials Science & Engineering, Washington University in St. Louis, St. Louis, MO 63130, USA

[‡]Department of Mechanical Engineering & Materials Science, Washington University in St. Louis, St. Louis, MO 63130, USA

[§]Center for Nanophase Materials Sciences, Oak Ridge National Laboratory, Oak Ridge, TN 37830, USA

[∥]Department of Chemical Engineering, University of Missouri, Columbia, MO 65211, USA

[⊥]Material Science and Technology Division, Oak Ridge National Laboratory, Oak Ridge, TN 37830, USA

[*]Corresponding author: rmishra@wustl.edu

[#]These authors contributed equally to this work.

Abstract

To evaluate the role of planar defects in lead-halide perovskites — cheap, versatile semiconducting materials — it is critical to examine their structure, including defects, at the atomic scale and develop a detailed understanding of their impact on electronic properties. In this study, we combine post-synthesis nanocrystal fusion, aberration-corrected scanning transmission electron microscopy, and first-principles calculations to study the nature of different planar defects formed in $CsPbBr_3$ nanocrystals. We observe two types of prevalent planar defects from atomic resolution imaging: previously unreported Br-rich [001](210)$\sum$5 grain boundaries and Ruddlesden-Popper planar faults. Our first-principles calculations reveal that neither of these planar faults induce deep defect levels, but their Br-deficient counterparts do. We find that the $\sum$5 grain boundary repels electrons and attracts holes, similar to an *n-p-n* junction, and the Ruddlesden-Popper planar defects repels both electrons and holes, similar to a semiconductor-insulator-semiconductor junction. Finally, we discuss the potential applications of these findings and their implications to understand the planar defects in organic-inorganic lead-halide perovskites that have led to solar cells with extremely high photoconversion efficiencies.

Keywords

Lead-halide perovskites, grain boundary, Ruddlesden-Popper fault, density-functional theory, scanning transmission electron microscopy

1. Introduction

Lead-halide perovskites, such as $CH_3NH_3PbI_3$ and $CsPbBr_3$, have recently emerged as a promising family of low-cost, high-performance semiconductors for a variety of applications including in solar cells, solid-state lighting, lasing, and photocatalysis.[1] The band gap of these perovskites can be tuned over a wide range for targeted applications by changing the cation or anion composition. Furthermore, they can be fabricated on a large scale over different substrates using low-cost solution-based methods.[2, 3] In traditional semiconductors, defects often deleteriously affect the performance and require the use of expensive accurately-controlled growth techniques to minimize the formation of defects. Conversely, in lead-halide perovskites, most point defects with low formation energies, such as vacancies, only give rise to shallow defect levels. Point defects, such as cation antisites and Pb interstitials, that lead to deep defect levels and nonradiative recombination centers have high formation energies and are only present in low concentrations.[4, 5] Therefore, the electronic properties of lead-halide perovskites are found to be comparatively robust to a large concentration of defects that generally accompany solution-based growth techniques used to grow them.[4-6] Nonetheless, their performance can still be substantially improved by careful control over these deep-level point defects. For instance, an extremely high-power conversion efficiency of 19.1% in large-area solar cells was recently demonstrated by growing formamidinium-lead-halide-based perovskites under iodine-rich conditions that minimized the concentration of the deep-level defects.[7]

Besides point defects, the solution-based growth also leads to polycrystalline materials with abundant grain boundaries (GBs) and other planar faults.[8, 9] There have been diverging experimental reports on the electrical activity of GBs in lead-halide perovskites. While some groups reported GBs to be electrically benign,[10] or even beneficial for charge transport,[11] others have shown that GBs act as nonradiative recombination centers and their passivation leads to improved carrier separation.[12-14] Atomic-scale modeling of hypothetical GBs—derived from analog of GBs in inorganic oxide perovskites, such as $SrTiO_3$, that have been characterized using scanning transmission electron microscopy (STEM) [15]—consistently predict them to be benign without inducing any deep-level defect states.[4, 16] However, because these lead-halide perovskites have a significantly larger lattice (>1.5 times) and different electronic structure relative to typical inorganic oxide perovskites, the similarity of their GBs remains an open question. Therefore, to understand the electrical and optical properties of GBs in lead-halide perovskites, there is a need for their atomic-scale imaging.

In this study, we have combined nanocrystal synthesis, STEM characterization, and first-principles modeling to investigate the planar defects in lead-halide perovskite nanocrystals. Given the sensitivity of organic-inorganic lead-halide perovskites to the electron beam in a TEM, we have investigated an inorganic perovskite $CsPbBr_3$, which is significantly more stable than the organic-inorganic lead-halide perovskites.[17] We have used a synthesis process that induces fusion of small nanocrystals to form planar defects.[18] Using STEM *Z*-contrast imaging, we find the presence of two dominant planar defects: high-angle GBs, such as a previously unreported Br-rich [001](210)$\sum$5 GB, and Ruddlesden-Popper (RP) planar faults. We have combined the atomic structure of these planar defects with density-functional theory (DFT) calculations to obtain their electronic properties. We reveal that the experimentally observed Br-rich GBs and RP planar faults do not induce deep defect levels, but their Br-deficient counterparts do. We predict that the dominant $\sum$5 GB repels electrons but attract holes, while the RP planar fault repels both electrons and holes. Therefore, both the planar faults are expected to affect charge transport and electron hole recombination in $CsPbBr_3$. Finally, we extend our results to GBs in organic-inorganic lead-halide perovskites to resolve the conflicting experimental reports on their activity.

2. Results and Discussions

Morphology of nanoparticles and planar defects. To carry out post-synthesis fusion of small nanocrystals to allow the formation of planar faults, we have used diethylzinc to remove the surface ligands on colloidally grown $CsPbBr_3$ nanocrystals. Within 48 hours, the nanocrystals grow from 8 to 59 nm in lateral dimensions. Further experimental details are provided in the Experimental and Modeling section. Depending on the relative position and surface termination of the nanoparticles, we find that the fusion of two nanoparticles can result in three types of planar defects: RP planar fault, symmetric GB, and asymmetric GB, as schematically shown in Figs. 1a, b, and c, respectively, together with the corresponding high-angle annular dark field (HAADF) images. In HAADF imaging, the contrast is approximately proportional to the square of the atomic number (*Z*),[20] allowing the atomic species to be identified by their *Z*-contrast as described later.

Previous studies[19] have shown that the surfaces of $CsPbBr_3$ nanocrystals are terminated with CsBr-rich planes under typical growth conditions. Therefore, it is expected that when two parallel nanocrystals with CsBr-rich (001) surfaces merge, a RP planar fault would be formed (Fig. 1a). If the contact surfaces of two nanocrystals are not parallel but have the same surface

termination (Fig. 1b), a symmetric GB could be formed after significant atomic rearrangement. If the two nanocrystal surfaces have different terminations, an asymmetric GB would be formed (Fig. 1c). The overall morphology of $CsPbBr_3$ nanocrystals before and after the fusion can be found in Section 1 of the Supporting Information.

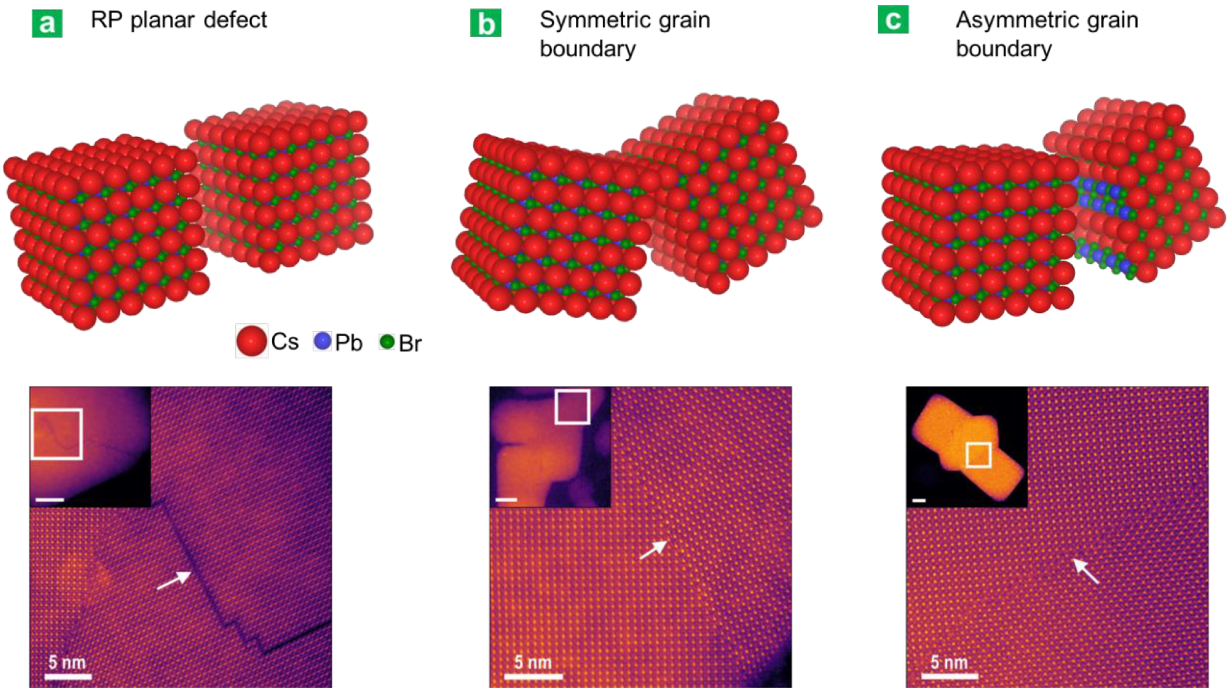

Figure 1. Schematic of formation of different planar faults during the fusion of $CsPbBr_3$ nanocrystals and their respective HAADF images: (a) RP planar fault, (b) symmetric GB, and (c) asymmetric GB. Each type of planar defect in these HAADF images is indicated with a white arrow. The insets show low magnification images of the fused nanocrystals.

Figures 2a and 2b show atomic-resolution HAADF images of a prevalent symmetric GB formed during the fusion process. HAADF images of other less common GBs can be found in Section 2 of the Supporting Information. In Fig. 2c, the atomic columns in Fig. 2b are labeled according to the histogram of the *Z*-contrast ($Z = 82$ for Pb, $Z = 55$ for Cs, and $Z = 35$ for Br), as shown in the inset of Fig. 2c. The atom-labelled image indicates that the out-of-plane orientation of this GB is $CsPbBr_3$ [001].

To verify our observations, we examine the GB structure from Fig. 2b and 2c using DFT calculations. The DFT-optimized structure shown in Fig. 2d is in good agreement with the HAADF image. For instance, in the DFT-optimized structure, the in-plane distance between two neighboring Pb atoms that are shared by both grains is 13.27 Å (marked as *a* in Fig. 2d) and the in-plane Pb–Br bond distance related to the shared Br atom (marked as *b* in Fig. 2d) is

3.04 Å, both of which match with the respective distances of 13.16 Å and 3.08 Å in the experimental image. The GB angle of 128.0º obtained from DFT also agrees well with the experimental angle of 127.3º. The simulated STEM image of the structure in Fig. 2d and its comparison with experimental image can be found in Section 3 of the Supporting Information. According to the coincidence-site-lattice model, we assign this GB as [001](210)∑5, where [001] denotes the out-of-plane crystalline direction and (210) denotes the plane parallel to the GB. The HAADF images and analyses of a less common asymmetrical ∑17 GB and several other types of GBs can be found in Section 2 of the Supporting Information.

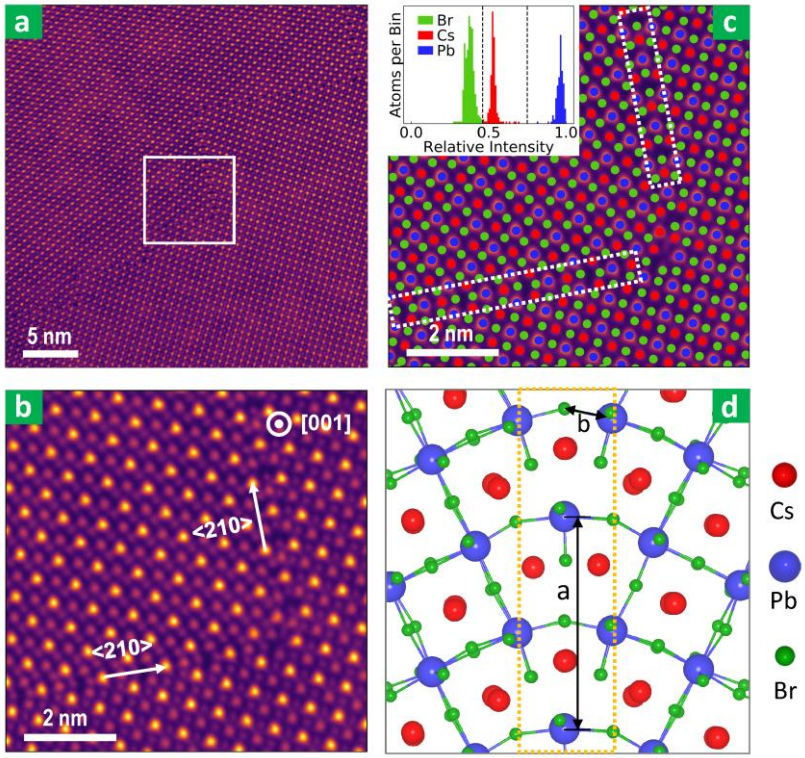

Figure 2. (a) HAADF image of a symmetrical GB, Br-rich [001](210) Σ5, found in $CsPbBr_3$ nanocrystals. (b) Atomic resolution HAADF image of a selected region as indicated by a white square in (a). (c) Atomic assignment of the structure in (b) according to the *Z*-contrast intensity of individual atomic columns and (d) the corresponding structure optimized using DFT computations. The distances *a* and *b* in (d) are 13.27 and 3.04 Å, respectively.

The structure of Σ5 GB discovered in this work is different from the previously known Σ5 GBs, both those derived from oxide perovskites and those proposed theoretically for lead-halide perovskites. For instance, the Br-rich GB found in this work (Fig. 3a) is different from the [001](210)Σ5 GB found in $SrTiO_3$[21] (Fig. 3b) and the proposed most stable theoretical GB in $CsPbX_3$ (Fig. 3c),[16] in terms of their Cs/Br stoichiometry. Figure. 3a is also significantly different from the [001](310)Σ5 GB reported in oxide perovskites[22] (Fig. 3d) and that

reported in $CH_3NH_3PbI_3$[23] and $CsPbBr_3$[16] (Fig. 3e). Our thermodynamic calculations under Br- and Cs-rich conditions show that the relative energy of GBs in Fig. 3a–3e is 0.1, 0.0, 3.9, 6.0, and 0.8 eV per shared Pb atom, respectively, which indicates that the structure in Fig. 3b would also be observed when the growth is close to thermal equilibrium, but the structures in Fig. 3c-3e are energetically unfavorable. This comparison demonstrates the necessity of combining STEM imaging and DFT calculations in resolving the GB structures of $CsPbBr_3$ under experimental conditions, which may not be necessarily under equilibrium.

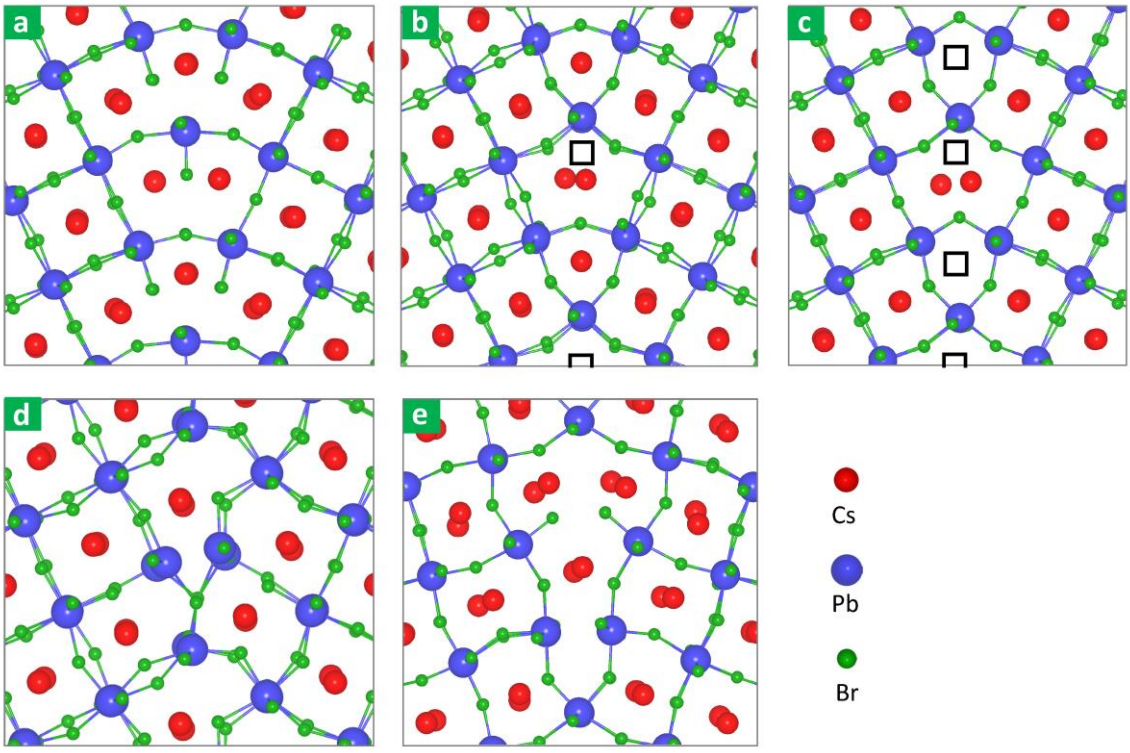

Figure 3. Comparison of various Σ5 GBs in $CsPbBr_3$: (a) [001](210)Σ5 GB discovered in this work, (b) [001](210)Σ5 GB inspired by Ref. [21], (c) [001](210)Σ5 GB from Ref. [16], (d) [001](210)Σ5 GB inspired by Ref. [21], and (e) [001](310)Σ5 GB from Ref. [16, 22, 23]. Blank squares in (b) and (c) correspond to vacancies relative to the structure in (a).

Another typical type of planar defects found in the fused nanocrystals are RP planar faults, which consists of two CsBr layers with rock-salt stacking sandwiched between two $CsPbBr_3$ domains on either side. Figure 4a shows that the RP planar fault can propagate along the (010) and (100) planes throughout the nanocrystals and form a 90° step at each intersection. An atomic resolution HAADF image of the RP planar fault is shown in Fig. 4b and the *Z*-contrast atomic assignment in Fig. 4c clearly shows the rock-salt stacking of CsBr bilayers. Our DFT-optimized atomic structure of the RP planar fault is shown in Fig. 4d. We find that the average

layer distance between the CsBr bilayer is predicted to be 3.70 Å by DFT, which is in good agreement with the experimental value of 3.59 Å based on analysis of the HAADF image in Fig. 4c. The rumpling of Br atoms in Fig. 4d is difficult to quantify from the HAADF image because the *Z*-contrast of Br atoms is too weak relative to the heavier cations, as confirmed by our simulated STEM image of Fig. 4d and its comparison with the experimental image (see Section 3 of the Supporting Information). Besides the noticeable RP planar faults observed in the (100) and (010) planes, we also notice the evidence of its formation in the (001) plane, similar to a previous observation in $CsPbBr_3$ nanosheets,[8] and a detailed analyses can be found in Section 4 of the Supporting Information.

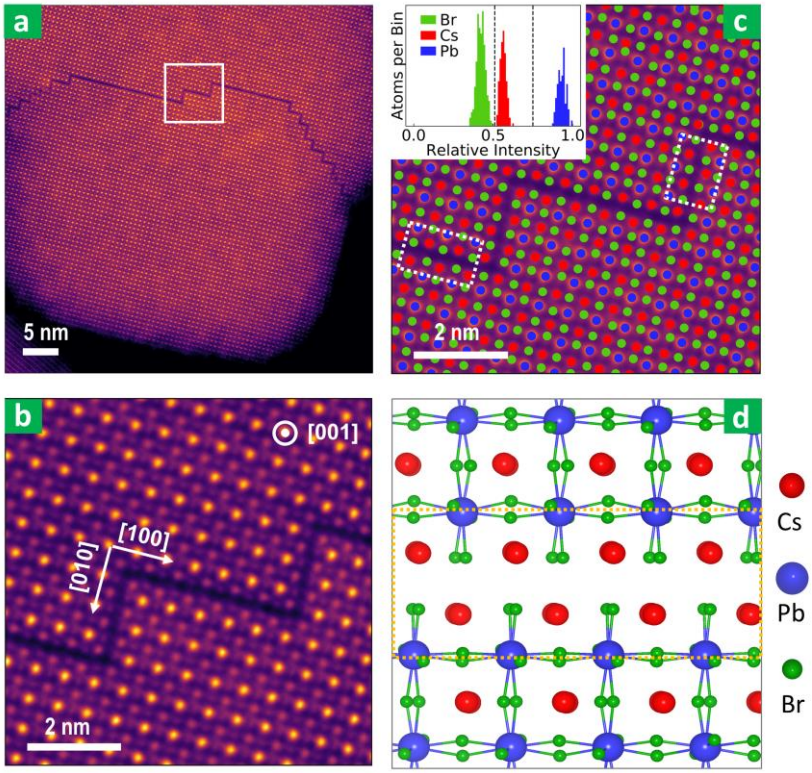

Figure 4. (a) Low-resolution HAADF image of RP planar faults propagating through two fused nanocrystals. (b) Atomic resolution HAADF image of a selected region indicated by the white square in (a). (c) Atomic assignment of the structure in (b) according to *Z*-contrast intensities. (d) Atomic model of the RP planar fault optimized using DFT.

Electronic properties of planar defects. In traditional semiconductors, planar defects often hinder charge transport and promote nonradiative recombination by inducing deep defect levels and/or charge barriers. Having obtained accurate atomic structures of GBs and RP planar faults in $CsPbBr_3$, we now investigate their impact on the electronic properties. Our DFT calculations indicate that neither the [001](210)$\sum$5 GB nor the RP planar fault introduces any defect levels in the band gap, as shown in the density of states (DOS) plots in Fig. 5a. Since planar defects

could serve as a sink for point defects and thus exhibit dynamic composition,[24-26] we have examined several additional structures by introducing Cs and/or Br vacancies to the experimentally confirmed ∑5 GB and RP planar fault. One example for the ∑5 GB is shown in Fig. 5b and a complete list can be found in Section 5 of the Supporting Information. Interestingly, we find that most structures still do not show any defect states in the band gap, except those involving Pb dangling bonds and/or Pb–Pb bonds, a phenomenon similar to that reported for point defects in $CsPbBr_3$.[27, 28] For instance, Br vacancies in the structure of Fig. 5b result in the formation of Pb–Pb bonds, which induce a deep defect level within the band gap (Fig. 5a) and localized electron density around the Pb–Pb bonds (Fig. 5b). These findings suggest that growth of $CsPbX_3$ under halogen-poor conditions should be avoided to minimize the deep defect levels induced by Pb dandling bonds or Pb-Pb bonds at GBs. We also examine the intersections formed by the [001](210)Σ5 GBs and RP planar defects (see kinks in Fig. 2 and 4) and find that these intersections do not introduce deep defect levels in the band gap, same as their straight counterparts (see Section 6 of the Supporting Information).

We have further examined the band diagram across the [001](210)∑5 GB and the RP planar fault to understand their effect on electron and hole transport. The band diagrams are obtained through a layer-by-layer projection of the density of states (LDOS) and are shown in Fig. 6a and 6b for the GB and the RP fault, respectively. We find that the ∑5 GB results in a relatively small band bending whereas the RP planar fault leads to a large band offset. Specifically, the conduction band offset ΔE_{CBM} and the valence band offset ΔE_{VBM} is 86 and 37 meV for the ∑5 GB, and 134 and -193 meV for the RP planar fault, respectively. Therefore, around room temperature (with a thermal energy of ~26 meV), the ∑5 GB repels electrons and partially attracts holes like that of an *n-p-n* junction, while the RP planar fault repels both electrons and holes like a semiconductor-insulator-semiconductor junction. The band offsets are consistent with the charge density of the VBM and CBM at the ∑5 GB and RP planar fault. As shown in Fig. 6c and 6d, the positive ΔE_{CBM} drives electrons away from both the ∑5 GB and the RP planar fault, while the positive ΔE_{VBM} of ∑5 GB attracts holes to it and the negative ΔE_{VBM} of RP planar fault repels holes away from it. The sharp change of ΔE_{CBM} versus smooth change of ΔE_{VBM} in RP planar fault (Fig. 6b) is also clearly observed in Fig. 6d.

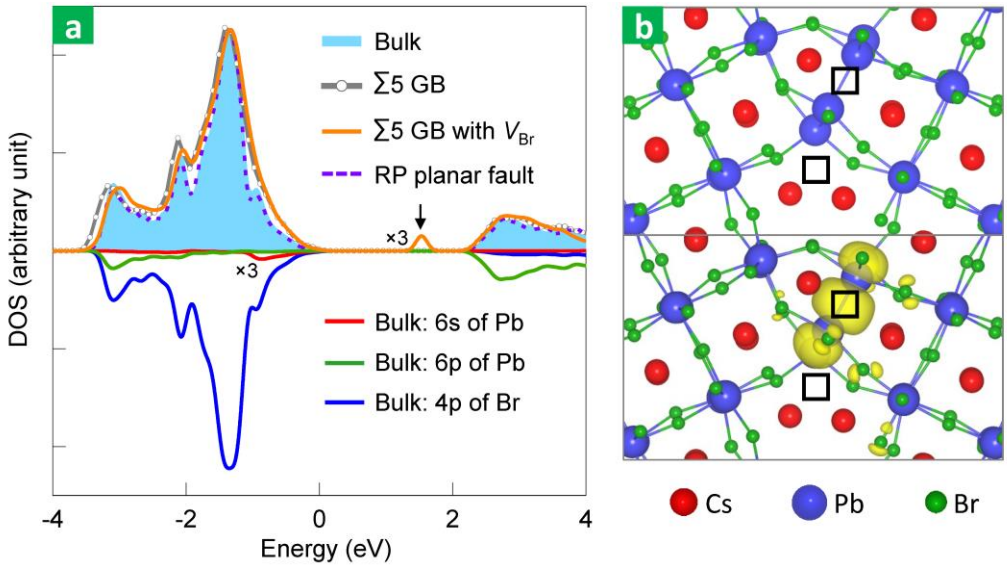

Figure 5. (a) Upper: comparison of DOS among bulk $CsPbBr_3$, the $\Sigma 5$ GB discovered in this work without and with V_{Br}, and the RP planar fault. The curves are magnified to match the highest peaks for easy comparison. Lower: orbital decomposition of the DOS of bulk $CsPbBr_3$. For easy visualization, the in-gap defect states of $\Sigma 5$ GB with V_{Br} and the curve corresponding to 6*s* of Pb have been magnified by three times. (b) Structure of $\Sigma 5$ GB with V_{Br} and electron density of its defect state indicated by arrow in (a). Blank squares in (b) correspond to vacancies relative to the Br-rich $\Sigma 5$ GB discovered in this work.

These band offsets can be qualitatively understood according to the composition of the planar defects and the band structure of $CsPbBr_3$. As shown in Figs. 5, 6c, and 6d, and previous literature,[28] the VBM of bulk $CsPbBr_3$ consists of antibonding states from 6*s* electrons of Pb and 4*p* electrons of Br, and the CBM consists of the antibonding states from the 6*p* electrons of Pb and 4*p* electrons of Br. Because the [001](210)$\sum$5 GB has a composition of $CsPbBr_{3+\delta}$, such Br-rich environment is expected to increase the antibonding interaction between Pb and Br, which increases the band gap and induces the positive ΔE_{VBM} and ΔE_{CBM} in Fig. 6a. Because the RP planar fault has a significantly different stoichiometry (CsBr) relative to $CsPbBr_3$, a similar perturbation-based understanding as of the $\sum$5 GB is invalid. However, we find that the band diagram of RP planar fault is closely related to that of $CsPbBr_3$/CsBr heterojunction, where the bulk CsBr induces a negative ΔE_{VBM} and positive ΔE_{CBM} relative to $CsPbBr_3$ (see Section 7 of Supporting Information).

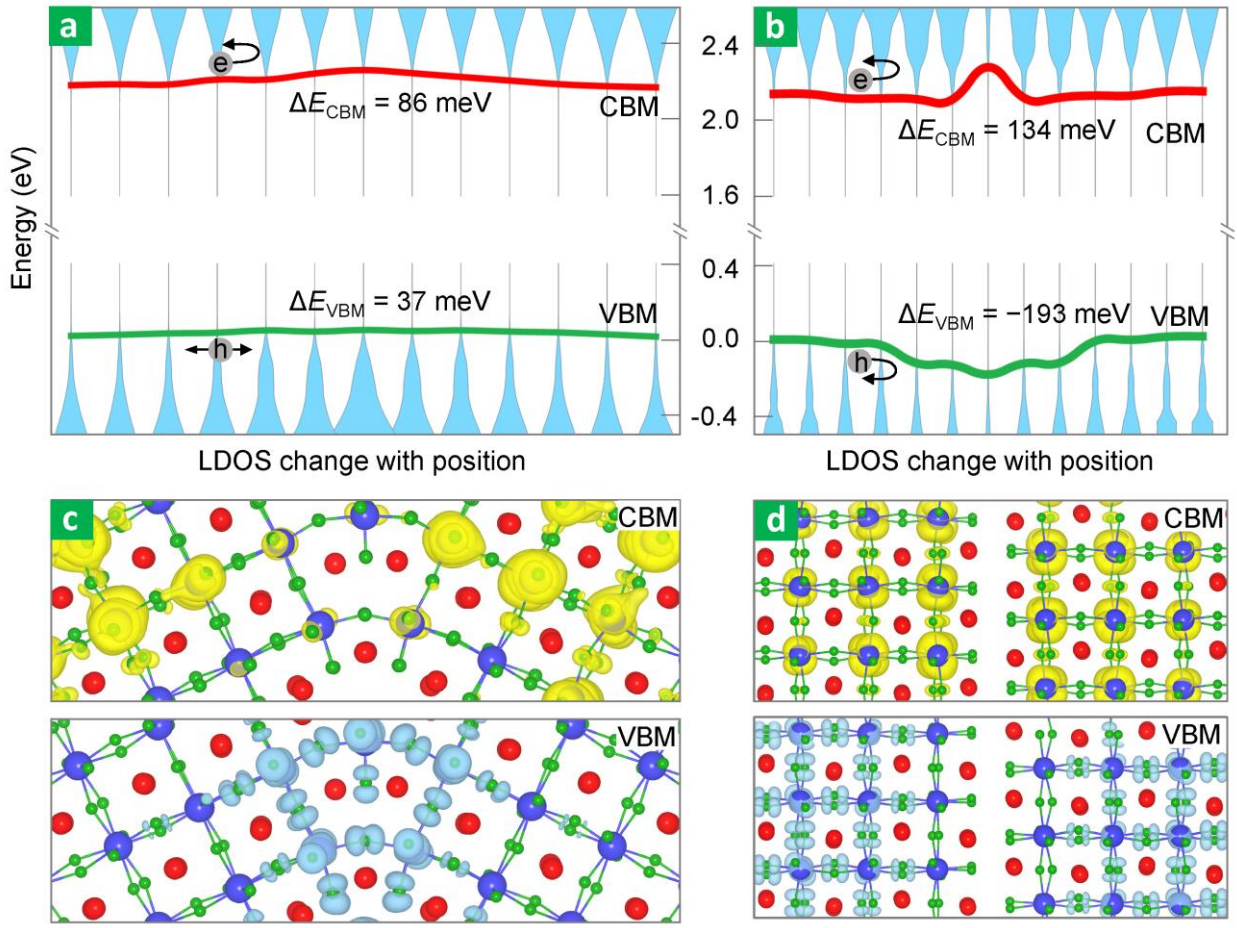

Figure 6. LDOS and band diagram of (a) the ∑5 GB and (b) RP planar fault. Charge density of CBM and VBM for the (c) ∑5 GB and (d) RP planar fault. For LDOS analyses, two neighboring atomic layers are chosen to contain the same integer number of $CsPbBr_3$ formula units, except at the planar defect. For band offset analyses, the band edge is picked as a LDOS constant to produce the band gap in the internal region.

Several implications can be anticipated based on the electronic properties of the [001](210)∑5 GB and RP planar fault. Since the ∑5 GB partially repels electrons but conducts holes relatively well, it could be engineered to reduce the thermal conductivity by increasing phonon scattering while retaining bulk-like hole conductivity, which may find application as *p*-type electrode in thermoelectric devices. Additionally, the ∑5 GB could help separate the electron-hole pairs in solar cells, similar to the GBs of CdTe solar cells.[29] For the RP planar fault, since it serves as an effective electron and hole barrier and naturally binds two $CsPbBr_3$ regions with a sharp interface, it could be utilized to impose strong quantum confinements in large nanocrystals.[18] Since both ∑5 GBs and RP planar defects exhibit noticeable upward bending for CBM, both the planar defects should be minimized for use of $CsPbBr_3$ in light-emitting devices, which

typically favor the type-I band diagram with downward bending for CBM and upward bending for VBM.

Implications for organic-inorganic lead-halide perovskites. In view of the structural similarities, our findings on $CsPbBr_3$ could help explain previous intriguing and diverging results about the role of GBs in organic-inorganic lead-halide perovskites. On one hand, local fluorescence lifetime imaging experiments have shown that the GBs of $CH_3NH_3PbI_3$ show lower photoluminescence (PL) intensity relative to the center of the grains.[13, 14] On the other hand, previous experiments based on Kelvin probe force microscopy and conductive-AFM found that GBs could benefit the charge separation and increase the photovoltage.[11] These seemingly conflicting results could be explained by the two aspects of GBs: defect levels and band offsets. As we have shown, the Br-rich [001](210)$\sum$5 GB does not exhibit deep defect levels but the Br-deficient ones do, which explains the low PL intensity at the GBs and significant improvement after halogen treatment.[7, 14] Since the halide-rich [001](210)$\sum$5 GB repels electrons but attracts holes, it could indeed help separate the excitons and increase the photovoltage.

3. Summary

In summary, we have combined nanocrystal synthesis, STEM characterization, and DFT calculations to systematically investigate two commonly observed planar defects in $CsPbBr_3$ nanocrystals: GBs and RP planar faults. We have revealed the structure of these two planar defects with atomic precision and showed that the GBs observed in the lead-halide perovskites are different from those in oxide perovskites. We find that both types of planar defects do not show deep defect levels as long as there are no Pb dangling bonds or Pb–Pb bonds, but they produce band offsets that are significant enough to impact the charge transport and electron-hole recombination. Our results thus disprove an assumption that since $CsPbBr_3$ are tolerant to many point defects, its planar defects would also have negligible impact on its electronic properties. Overall, by elucidating the atomic and electronic structure of the GBs and RP planar faults under real growth conditions, our findings provide a path to controlling and even engineering these faults to achieve the full potential of $CsPbBr_3$ in particular, and lead-halide perovskites in general.

Experimental and Modelling Details

Nanocrystal growth. $CsPbBr_3$ nanocrystals were synthesized using a hot-injection technique, as described by Protesescu *et al*.[2] Diethylzinc was then used to fuse these as-synthesized

nanocrystals to form larger nanocrystals. 0.2 M diethylzinc in anhydrous *n*-heptane solution was injected to the as-synthesized $CsPbBr_3$ nanocrystals in a glovebox under Ar atmosphere at room temperature. We found that 5 wt. % of diethylzinc lead to enhanced fusion growth of the nanocrystals with relatively uniform size distribution. After the injection of diethylzinc, the nanocrystal colloid solution was stirred for 1 min in the glovebox and was subsequently diluted with anhydrous *n*-heptane in 1:10 volume ratio in ambient air. More details can be found in our previous work focusing on fusion growth of these nanocrystals.[18]

STEM characterization. The STEM experiments were carried out using the aberration-corrected (equipped with fifth-order aberration corrector) Nion UltraSTEM^{TM} 200 (operated at 200 kV) and Nion UltraSTEM^{TM} 100 (operated at 100 kV) at Oak Ridge National Laboratory. Gaussian blurring was used to smooth out the HAADF images to accurately determine the position of the respective atomic columns. The nanocrystals were deposited on a carbon support TEM grid by drop casting. The grids were heated to 160 ºC in vacuum to remove surface impurities prior to STEM experiments. The in-plane lattice constants for the HAADF image are calibrated to 8.49 and 8.15 Å, which are the refined lattice constants of $CsPbBr_3$ nanocrystals with an edge length of 12.5 nm obtained from Ref. [30].

Computational details. Our first-principles modeling is based on DFT, as implemented in the Vienna *Ab initio* Simulation Package.[31] We have used the Perdew–Burke-Ernzerhof[32] exchange-correlation functional. The plane-wave energy cutoff was set to 400 eV and the projector augmented wave method[33] was utilized with the following potentials: Cs_sv_GW($5s^25p^66s^1$) for Cs, Pb_d_GW($5s^25d^{10}6s^26p^2$) for Pb, and Br_GW($4s^24p^5$) for Br. We adopted the orthorhombic structure of $CsPbBr_3$ as confirmed for its nanocrystals.[30] The supercell size of the $\sum 5$ GBs is about 11.8 × 13.3× 75.9 $Å^3$ and the RP planar fault is 8.2 × 8.5 × 90.2 $Å^3$. We sampled the Brillouin zone using Monkhorst-Pack *k*-points grid of 3 × 3 × 1 and 4 × 4 × 1 for the GB and the RP fault, respectively. Two or three atomic layers parallel to the planar defect were fixed to their bulk positions to simulate the internal region of grains, while the remaining atoms were relaxed till the force on each atom is less than 0.01 eV/Å. The optimized structures mentioned in the main text and Supporting Information can be found in the Supplementary Data Set.

Acknowledgements

RM acknowledges support through the Ralph E. Powe Junior Faculty Enhancement Award from Oak Ridge Associated University and National Science Foundation (NSF) grant DMR-

1806147. A portion of the STEM experiments was conducted at the Center for Nanophase Materials Sciences at Oak Ridge National Laboratory (ORNL), which is a Department of Energy (DOE) Office of Science User Facility, through a user project (AST, JAH, JCI, and RM). AYB was supported by the Division of Materials Science and Engineering, US DOE. This research was conducted, in part, using instrumentation within ORNL's Materials Characterization Core provided by UT-Battelle, LLC under Contract No. DE-AC05-00OR22725 with the U.S. Department of Energy. This work used the computational resources of the Extreme Science and Engineering Discovery Environment (XSEDE), which is supported by NSF grants ACI-1053575 and ACI-1548562.

Conflict of Interest

The authors declare no conflict of interest.

Reference

[1] C. C. Stoumpos, M. G. Kanatzidis, Adv. Mater. 2016, 28, 5778.

[2] L. Protesescu, S. Yakunin, M. I. Bodnarchuk, F. Krieg, R. Caputo, C. H. Hendon, R. X. Yang, A. Walsh, M. V. Kovalenko, Nano Lett. 2015, 15, 3692.

[3] Q. A. Akkerman, V. D'Innocenzo, S. Accornero, A. Scarpellini, A. Petrozza, M. Prato, L. Manna, J. Am. Chem. Soc. 2015, 137, 10276.

[4] W. J. Yin, T. Shi, Y. Yan, Adv Mater 2014, 26, 4653.

[5] W.-J. Yin, T. Shi, Y. Yan, Appl. Phys. Lett. 2014, 104, 063903.

[6] A. Buin, R. Comin, J. Xu, A. H. Ip, E. H. Sargent, Chem. Mater. 2015, 27, 4405; J. Kang, L. W. Wang, J Phys Chem Lett 2017, 8, 489.

[7] W. S. Yang, B. W. Park, E. H. Jung, N. J. Jeon, Y. C. Kim, D. U. Lee, S. S. Shin, J. Seo, E. K. Kim, J. H. Noh, S. I. Seok, Science 2017, 356, 1376.

[8] Y. Yu, D. Zhang, P. Yang, Nano Lett. 2017, 17, 5489.

[9] L. Gomez, J. Lin, C. de Weerd, L. Poirier, S. C. Boehme, E. von Hauff, Y. Fujiwara, K. Suenaga, T. Gregorkiewicz, ACS Appl. Mater. Interfaces 2018, 10, 5984.

[10] E. Edri, S. Kirmayer, S. Mukhopadhyay, K. Gartsman, G. Hodes, D. Cahen, Nat. Commun. 2014, 5, 3461.

[11] J. S. Yun, A. Ho-Baillie, S. Huang, S. H. Woo, Y. Heo, J. Seidel, F. Huang, Y.-B. Cheng, M. A. Green, J. Phys. Chem. Lett. 2015, 6, 875.

[12] J. Xu, A. Buin, A. H. Ip, W. Li, O. Voznyy, R. Comin, M. Yuan, S. Jeon, Z. Ning, J. J. McDowell, P. Kanjanaboos, J. P. Sun, X. Lan, L. N. Quan, D. H. Kim, I. G. Hill, P. Maksymovych, E. H. Sargent, Nat. Commun. 2015, 6, 7081.

[13] N. De Marco, H. Zhou, Q. Chen, P. Sun, Z. Liu, L. Meng, E. P. Yao, Y. Liu, A. Schiffer, Y. Yang, Nano Lett. 2016, 16, 1009.

[14] D. W. deQuilettes, S. M. Vorpahl, S. D. Stranks, H. Nagaoka, G. E. Eperon, M. E. Ziffer, H. J. Snaith, D. S. Ginger, Science 2015, 348, 683.

[15] M. Kim, G. Duscher, N. D. Browning, K. Sohlberg, S. T. Pantelides, S. J. Pennycook, Phys Rev Lett 2001, 86, 4056; T. Mizoguchi, Y. Sato, J. P. Buban, K. Matsunaga, T. Yamamoto, Y. Ikuhara, Appl. Phys. Lett. 2005, 87, 241920.

[16] Y. Guo, Q. Wang, W. A. Saidi, J. Phys. Chem. C 2017, 121, 1715.

[17] M. Kulbak, D. Cahen, G. Hodes, J. Phys. Chem. Lett. 2015, 6, 2452.

[18] Maria V. Morrell, Guangfu Luo, Arashdeep S. Thind, Tommi A. White, Jordan A. Hachtel, Albina Y. Borisevich, Juan-Carlos Idrobo, Rohan Mishra, Yangchuan Xing, ACS Appl. Nano Mater. 2018, DOI: 10.1021/acsanm.8b01298.

[19] S. Wei, Y. C. Yang, X. J. Kang, L. Wang, L. J. Huang, D. C. Pan, Chem. Commun. 2016, 52, 7265; S. ten Brinck, I. Infante, ACS Energy Lett. 2016, 1, 1266.

[20] S. J. Pennycook, D. Jesson, Ultramicroscopy 1991, 37, 14.

[21] M. Kim, G. Duscher, N. D. Browning, K. Sohlberg, S. T. Pantelides, S. J. Pennycook, Phys. Rev. Lett. 2001, 86, 4056.

[22] M. Imaeda, T. Mizoguchi, Y. Sato, H. S. Lee, S. D. Findlay, N. Shibata, T. Yamamoto, Y. Ikuhara, Phys. Rev. B 2008, 78, 245320.

[23] W. J. Yin, T. Shi, Y. Yan, Adv. Mater. 2014, 26, 4653.

[24] J. H. Jang, Y. M. Kim, Q. He, R. Mishra, L. Qiao, M. D. Biegalski, A. R. Lupini, S. T. Pantelides, S. J. Pennycook, S. V. Kalinin, A. Y. Borisevich, ACS Nano 2017, 11, 6942;

[25] J. Gazquez, R. Guzman, R. Mishra, E. Bartolome, J. Salafranca, C. Magen, M. Varela, M. Coll, A. Palau, S. M. Valvidares, P. Gargiani, E. Pellegrin, J. Herrero-Martin, S. J. Pennycook, S. T. Pantelides, T. Puig, X. Obradors, Adv. Sci. 2016, 3, 1500295;

[26] M. A. Frechero, M. Rocci, G. Sanchez-Santolino, A. Kumar, J. Salafranca, R. Schmidt, M. R. Diaz-Guillen, O. J. Dura, A. Rivera-Calzada, R. Mishra, S. Jesse, S. T. Pantelides, S. V. Kalinin, M. Varela, S. J. Pennycook, J. Santamaria, C. Leon, Sci Rep 2015, 5, 17229.

[27] H. Shi, M.-H. Du, Phys. Rev. B 2014, 90, 174103.

[28] J. Kang, L. W. Wang, J. Phys. Chem. Lett. 2017, 8, 489.

[29] C. Li, Y. L. Wu, J. Poplawsky, T. J. Pennycook, N. Paudel, W. J. Yin, S. J. Haigh, M. P. Oxley, A. R. Lupini, M. Al-Jassim, S. J. Pennycook, Y. F. Yan, Phys. Rev. Lett. 2014, 112.

[30] P. Cottingham, R. L. Brutchey, Chem. Commun. 2016, 52, 5246.

[31] G. Kresse, J. Furthmuller, Phys. Rev. B 1996, 54, 11169.

[32] J. P. Perdew, K. Burke, M. Ernzerhof, Phys. Rev. Lett. 1996, 77, 3865.

[33] P. E. Blöchl, Phys. Rev. B 1994, 50, 17953.